2016-08

On the use of the Radon transform to estimate longshore currents from video imagery

Almar, R

http://hdl.handle.net/10026.1/8049

On the use of the Radon transform to estimate longshore currents from video imagery

Rafael Almar[1,*], Stanislas Larnier[2], Bruno Castelle[3], Timothy Scott[4], France Floc'h[5]

Abstract

A direct estimation of longshore currents using in-situ instruments is difficult and costly, and often limited to punctual measurements over short durations. Video remote sensing systems offers an alternative when drifting features, like foam induced by breaking waves or other streaks, are visible. In this paper we describe a method based on the application of the Radon transform on longshore spatio-temporal images. The sinogram from the Radon transform is used to find the angle of the drifting, further converted into current. Our approach is first tested using synthetic fields created using anisotropic Gaussian random currents and waves. Comparison is also made with in-situ currents from the Grand Popo 2014 experiment in Benin (Gulf of Guinea, West Africa). Results show an overall good agreement (O(30%)) in the swash, surf and inner shelf zones while the method offers best skills in the surf zone (17%) where the drifting foam induced by wave breaking is evident. The width of the Radon peak is found to be a good proxy of accuracy. This remote sensing method allows a long term monitoring of the longshore current and its cross-shore structure, which brings new perspectives in quantifying sediment drift variability.

Keywords: Nearshore, Video imagery, anisotropic Gaussian random fields,

---
[*]Corresponding author
  Email address: `rafael.almar@ird.fr` (Rafael Almar)
[1]IRD-LEGOS (CNRS/Univ. Toulouse/IRD/CNES), Toulouse, France
[2]CNRS-LAAS, Toulouse, France
[3]EPOC (CNRS/Univ. Bordeaux), Bordeaux, France
[4]University of Plymouth, UK
[5]LDO-IUEM, Brest, France

Remote sensing, Grand Popo, Benin

---

1. Introduction

Longshore current has attracted a major attention in the nearshore science for decades, generally within the scope of estimating longshore sediment transport (Komar, 1998). It is generated by oblique breaking waves, is rather vertically uniform and can reach values up to meter per second (Komar & Inman, 1970; Lippmann, 1970). Observations have shown that longshore current peaks at the location of the maximum of breaking and can present a multi-modal structure in case of barred beach (Schoonees & Theron, 1993; Putrevu & Svendsen, 1995; Haller & Svendsen, 2002; Feddersen, 2014). Tidal modulation of wave breaking and subsequent longshore current can be large, in particular at low tide terrace and barred beaches (Thornton & Guza, 1986; Feddersen, 2003), and intense current (> 0.5 m/s) have shown to present a substantial variability at low frequency scales (minutes), likely explained by shear instabilities (Allen et al., 1996; Oltman-Shay et al., 1989). At longer term, seasonal to inter-annual fluctuations are likely to be induced by wave conditions modulation due to climatic modes (Splinter et al., 2012; Almar et al., 2015). Suited documentation on its multi-scale spatio-temporal evolution has long been hampered by difficulties in measuring such fluctuating structures by conventional in-situ instrument arrays, while the application of recent shore-based remote sensing methods has a large potential.

Radars and video imagery have proved to be very efficient tools in monitoring the nearshore and in particular the surface current (Holman & Haller, 2013), for a reasonable running cost and over typical areas of kilometers and footprint of meters. Radar-based Doppler effect of backscattered signal from rough surface (Haller & Svendsen, 2014) is probably the most direct way in estimating surface currents. Video systems have been developed for over twenty years (Holman & Haller, 2013). From their incomparable low cost (< 1000 eur) and intuitive use, video stations are rapidly growing over world coasts, including developing coun-

tries, offering the exciting potential of an unequaled documentation of coastal zones from local to regional scale (Mole et al., 2013). Video methods were applied originally to estimate submerged and intertidal bathymetry (Lippmann & Holman, 1990; Stockdon & Holman, 2000) and time-varying location of the shoreline (Plant & Holman, 1997). Following the improvement of sensors resolution, an increasing number of methods have been developed recently to quantify wave's characteristics (Lippmann & Holman, 1991; De Vries et al., 2011; Stockdon & Holman, 2000; Almar et al., 2012) but only a few were dedicated to surface currents (Holman & Haller, 2013), though its key importance.

In this paper, we are interested in estimating the longshore current from video, in a similar way to (Chickadel et al., 2003). This contrasts with the two-dimensional approach based on a Particle Image Velocimetry (PIV) method (Holland et al., 2001; Puloe et al., 2003) generally applied in laboratory experiments (Cox & Anderson, 2001; Kimmoun & Branger, 2007) because it requires high temporal and spatial resolutions. Our choice of a one-dimensional approach rises from the availability of video spatio-temporal images (also called Hovmoller diagram or timestack) widely used to conserve high frequency information of cross-shore and longshore waves and current components, avoiding saving the whole high frequency video, which is particularly pertinent for long term monitoring. The second interest is because spatio-temporal format is perfectly suited for angle separation methods based on the Radon transform (RT, (Radon, 1917)). The RT has recently been successfully applied to ocean waves, in particular for the detection of ship wave (Copeland et al., 1995) and more recently to nearshore wave dynamics (Yoo et al., 2011; Almar et al., 2014a) and swash (Yoo et al., 2009) but no attempt was conducted to estimate the longshore current, despite the high potential of use.

In the next section our method is tested over synthetic data and field observation from Grand Popo, Benin (Gulf of Guinea, West Africa). The Bight of Benin is subject to increasing erosion due to anthropic perturbation of the strong longshore sediment transport (approximately 500.000 m^3/yr, (Almar et al., 2015)) exacerbated by the rapid development of deep water harbors in the main cities

3

from Accra to Lagos. Observing and quantifying this longshore drift is crucial

here to improve coastal zone management. The RT algorithm is described in

the first section and the synthetic and field datasets used in this paper are pre-

sented in the second section. In third section, the method's skills are tested

against these synthetic and field data, an application is provided to illustrate

the potential of the method and finally some concluding remarks are given.

2. Radon transform and algorithm

2.1. Radon transform

The Radon transform (Ramm & Katsevich, 1996; Mallat, 2008; Feeman,

2010) $R(\rho, \theta)$ over a bi-dimensional field $\mu(x, y)$ can be defined as:

$$R(\rho, \theta) = \oiint \mu(x,y)\delta(x\cos(\theta) + y\sin(\theta) - \rho)dxdy \qquad (1)$$

where δ is the Dirac delta function, θ and ρ are respectively the angle and

distance from origin of the integration line defined as $\rho = x\cos(\theta) + y\sin(\theta)$.

The origin is the center of the two-dimension field. The Radon transform $R(\rho, \theta)$

is defined for all possible values of θ from [0 to 180°] and ρ from 0 to the diagonal

length.

[Figure 1 about here.]

The Figure 1 shows the application of the RT to a disk and inclined lines.

The projection of a disk in Figure 1.a has a constant density at all angles while

the projection of the lines in Figure 1.d has two peaks, indicating their angles

θ.

[Figure 2 about here.]

2.2. Orientation detection algorithm

Figure 2 illustrates the application of the RT to a realistic video longshore

timestack (120×120 pixels, with spatial and temporal resolution of $dx = 0.25$

m/pix and $dt = 0.5$ s/pix respectively. Figure 2.a shows the raw image where

4

85 both wave crests and drifting foam can be seen. A high-pass radius filter (run-

86 ning average) is applied in the polar space to isolate highly-textured small-scale

87 foam streaks and remove signal longer than a threshold (here $\rho < 20$ points)

88 associated to water background intensity value, remaining foam and long wave

89 crests. Figure 2.b shows the resulting image used to determine the orientation

90 of the current. Figure 2.c shows the RT of the image in Figure 2.a where prop-

91 agating features are clearly visible as local maxima. RT resolution increases for

92 oblique angles around $45°$; it is recommended that the user adapt either spatial

93 or temporal resolution in order not to squeeze signal at $0°$ or $90°$ (horizontal

94 or vertical lines). The maximum of variability in the polar domain provides

95 the dominant propagation angle θ (see previous section), which can be further

96 converted into current velocity $V = \tan(\theta)dx/dt$, where dx and dt are spatial

97 and temporal resolution, respectively. V stands for the dominant velocity of the

98 features over the image. Noteworthy, a localized RT or local maxima detection

99 can be applied to retrieve the velocity $V(x,t)$ of individual features.

100 **3. Data**

101 *3.1. Synthetic cases*

102 In order to perform a first validation of a current orientation detection algo-

103 rithm, it is possible to simulate synthetic longshore timestacks (Chickadel et al.,

104 2003). The approach proposed in this article is based on anisotropic Gaussian

105 random fields.

106 The Matlab code titled "Generation of Random, Autocorrelated, Periodic

107 Fields" by Cirpka, O.A., available online on http://m2matlabdb.ma.tum.de was

108 used to create anisotropic Gaussian random fields. The method utilizes the

109 fact that the Fourier transform of the covariance function is the power spectral

110 density function of all realizations. Random autocorrelated fields are generated

111 by creating random phase spectra meeting the conditions of real numbers in

112 the physical domain. The realizations are then given by back-transformation of

113 the power- and phase-spectrum into the physical domain. Since the method is

5

based on the discrete Fourier transformation, the generated fields are periodic rather than stationary.

The synthetic cases generated for this paper have 100×100 pixels size, Gaussian laws of mean 0 and variance 10. Figures 6.a-c present one synthetic case created with our approach. Figure 6.a shows a first anisotropic Gaussian random field representing the foam pattern. The anisotropy can be compared to an ellipse with a major and minor axes, which are described here by correlation lengths of the signal in x and y, and an orientation θ. If the ratio of correlation lengths decreases, the ellipse is more elongated and the anisotropy increases. The correlation lengths in Figure 6.a are 20 and 2 pixels in x and y, respectively. The orientation is $\theta = 55°$ A second anisotropic Gaussian random field is shown in Figure 6.b representing the incoming waves with correlation lengths in x and y of 50 and 2 pixels, respectively. The orientation of the wave field is $\theta = 0°$. In Figure 6.c, they are combined to obtain a realistic test case.

Based on this initial wave-current field, Figures 6.d-f illustrate the influence of the correlation length ratio on the anisotropic Gaussian current fields. The correlation length ratio are 0.05, 0.15 and 0.25. Foam anisotropy decreases when correlation length increases, making streaks angle less evident.

To take into account for different levels of drifting streaks signature with waves and lighting conditions, an intensity threshold is applied. In Figures 6.f-h, the level of kept information are described by the percentage of pixels not changed, 30%, 50% and 70%, respectively. The lower the percentage of kept information is, the weaker are the foam streaks and more difficult their detection.

3.2. Field observations

The Bight of Benin(Figure 3) is a sandy open wave-dominated microtidal environment exposed to long period swells (ECMWF Erainterim reanalyse 1979-2013 annual deep water wave averages: H_s=1.36 m, T_p=9.4 s, Dir=$S - SW$, see Dee (2011)) generated at high latitudes in the South Atlantic. The beach (Figures 2 and 3) presents an longshore-uniform low tide terrace and a steep

6

upper shoreface. An eastward littoral drift of 0.8 to 1.5 m^3/yr has been reported in the literature (Anthony & Blivi, 1999; Blivi et al., 2014), driven by year-round oblique long swells (Almar et al., 2015).

A field experiment was conducted at Grand Popo beach (6.2°N, 1.7°E, Figure 3) from 10 to 18 March 2014 (Almar et al., 2014b). Inner shelf waves and currents were measured using an Acoustic Doppler Current Profiler (ADCP) moored in 10-m depth. Every day, various drifters releases were conducted in the surfzone around mid-tide to determine longshore current variability (Castelle et al., 2014). An Acoustic Doppler Velocimeter (ADV) was deployed in the swash zone during daylight hours. Hourly wind observations are provided by Cotonou airport, 80-km distant from Grand Popo and 500 m from the shore (i.e. sea breeze is observed). Figure 8 shows that during the experiment, tide varied from neap to spring tidal ranges, from 0.3 m to 1.2 m, respectively). Waves were energetic and relatively long (1.2 m $< Hs <$ 1.6 m and $Tp = $ 10-12 s), with initial higher waves (up to 1.8 m), coming from south-west, generating consistent eastward longshore currents. Surf zone longshore current varied from 0.4 m/s to 0.8 m/s, inner shelf current from 0.05 to 0.3 m/s, and swash current from 0 to 0.5 m/s.

A long-term video camera VIVOTEK IP7361, 1600x1200 pixels (Figure 3.c) was deployed in February 2013 (Almar et al., 2014b) on a 15 m-high semaphore belonging to the navy of the Republic of Benin, 80-m distant from the shore (i.e. which is the approximate beach width). During the experiment, full 2-Hz videos were stored. Rectification of images from pixels into real world coordinates was accomplished by direct linear transformation using GPS ground control points (Holland et al., 2013) after a correction of the lens radial distortion (Heikkila & Silven, 1997) (Figure 3.d). Although varying somewhat throughout the field of view, the pixel footprint was less than 0.1 and 0.05 m in the region of interest (surf-swash zones of the instrumented zone) for cross-shore and longshore direction, respectively (Figure 4). In the video data, the location of swash and surf zones were estimated from 10-min averaged cross-shore pixel intensity timestacks; the location of the surf being estimated as the maximum

7

175 of breaking-induced intensity and the swash as the transition between the beach

176 and surf (see illustration in Figure 5). Inner shelf video point is chosen constant,

177 close to the location of the ADCP. For the use of the RT, 100-m long longshore

178 spatio-temporal images (Figure 4) are reinterpoled on a regular grid of 0.25 m

179 and separated into subwindows of 5 m (see sensitivity analyze of the RT on res-

180 olution and windows size in Section 4.2), for resulting sub-images of 20 pixels

181 in space and 120 pixels in time and a regular spatial grid of 5 m both in the

182 cross-shore and longshore directions.

183   [Figure 3 about here.]

184   [Figure 4 about here.]

185   [Figure 5 about here.]

186   [Figure 6 about here.]

187 **4. Results and discussion**

188 *4.1. Tests on synthetic data*

189   A numerical study is performed to determine the sensitivity of the method's

190 skill on the drifting streaks anisotropy, intensity and orientation (i.e. velocity).

191 Numerous synthetic realistic timestacks are generated to cover a wide range of

192 conditions. Figure 7 presents the results of the sensitivity analysis. Figure 7.a

193 shows that method's skills increase with anisotropy (and decrease with correla-

194 tion length ratio) of the Gaussian random current fields. Figure 7.b shows that

195 the threshold value on the current field has not a substantial influence, which

196 indicates that the method is able to detect weak drifting streaks, as encountered

197 offshore of the surf zone. Results in Figure 7.c show that the orientation affects

198 the estimation, with a better accuracy at oblique angles close to 45°.

199   [Figure 7 about here.]

8

4.2. Comparison with in-situ measurements

201 Figures 8 and 9 show that video and in-situ currents are in good agreement,
202 with a RMS error of 0.07 m/s (35%, $R^2 = 0.65$, significant at the 95% level).
203 RMS errors are 0.06 m/s (17%), 0.09 m/s (44%) and 0.07 m/s (29%) for the
204 surf, swash and inner shelf zones, respectively. The RT method offers better
205 skills in the surf zone because of clear drifting foam (Figure 4) but is able to
206 estimate the current at more challenging zones where optical signature is weaker:
207 oscillating drift in the swash and turbidity streaks at the inner shelf. These
208 results show the ability of the RT-based method in estimating the whole cross-
209 shore profile of longshore surface current with a better spatial and temporal
210 resolution than any in situ deployment, though accuracy is lower (O(30%)).
211 Figure 10.a shows that the error is linked to the width of the RT peak width
212 in the polar space (correlation coefficient of 0.42, significant at 95% level), the
213 uncertainty increasing with the peak width. This can be used as a proxy to
214 discard estimates with large uncertainties encountered for afternoon sea breeze
215 or sun glint. Figure 10.b shows that the choice of the spatial dimension has
216 only a minor influence. In the contrary, the method accuracy increases with
217 resolution. The resolution might explain part of the errors in the inner shelf,
218 where the pixel footprint worsen to 1-2 m/pixel (Figure 4). Finally, even if
219 the main source of discrepancy can be attributed to the video method itself
220 and geometrical characteristics, in-situ data can cause some spreading in our
221 results, though it is difficult to quantify. Some studies reported accuracy of 0.01
222 to 0.5 m/s (MacMahan et al., 2009) for instant drifter velocities, which is largely
223 reduced by our hourly averaging. The longshore current is considered vertically
224 uniform. However, some discrepancies may arise between video estimate at
225 the surface and in-situ measurements in the water column: 35-cm and 1-m
226 average from the surface for the ADCP and the drifters, respectively, and a few
227 centimeters above the bed for the swash ADV.

228 To illustrate the potential of our method, Figure 11 shows its application
229 to the cross-shore structure of the longshore current. Video-derived profile in
230 Figure 11.a shows a good agreement with in-situ measurements, peaking in the

9

231 surf zone and extending to the inner shelf. Swash, surf and inner shelf currents

232 have different behavior. A multiple linear regression with the main forcing

233 (longshore wave energy flux, tide and wind) was conducted over the experiment

234 duration (hourly averaged, when video estimates are available). The relative

235 contribution of each forcing was computed as the ratio of individual variability

236 (variance) over the total reconstructed variance by the multiple liner regression.

237 Figure 8 shows that the swash is dominantly influenced by tidal modulation

238 (40%) of wave action rather than by offshore wave height (30%), certainly due

239 to tidal modulation of surf zone saturation; surf zone is as expected largely

240 dominated by wave action (65%) and wind dominates (20%) at the inner shelf.

241 The decrease of the total reconstructed signal with the distance to the shore

242 (from 90 % in the surf to 25 % on the shelf) denotes the difficulties in retrieving

243 the surface current with decreasing pixel resolution and less drifting features,

244 but also suggests a complex transitional zone behavior, influenced by both inner

245 shelf and nearshore processes. This difference of forcing for the three zones has

246 considerable implications in terms of longshore sediment drift. The possibility

247 of using the RT to estimate longshore current clearly provides new perspectives

248 in quantifying the longshore sediment drift and its variability.

249 [Figure 8 about here.]

250 [Figure 9 about here.]

251 [Figure 10 about here.]

252 [Figure 11 about here.]

253 **5. Conclusions**

254 Our understanding of the nearshore longshore current has been hampered

255 for long by the lack of adapted tool. This article presents a new approach to

256 estimate longshore currents from video spatio-temporal fields using the Radon

257 transform, recently applied to waves (Almar et al., 2014a). It is an alternative

10

to other approaches in one (Chickadel et al., 2003) and two dimensions (Holland et al., 2001). The Radon transform is tested and validated on synthetic and field data collected during the Grand Popo 2014 (Benin, West Africa) experiment. A sensitivity analyze using synthetic data shows that method's skills improve with streaks anisotropy and for oblique orientation close to 45 ° but stays fairly insensitive to the level of streaks signature. Comparison with field data shows a good agreement (O(30%)) in the swash, surf and inner shelf zones with RMS errors of 0.06 m/s (17%), 0.09 m/s (44%) and 0.07 m/s (29%), respectively. Error worsen when resolution decreases and Radon transform polar density peak enlarges. A first application of this method shows that during the experiment, swash, surf and inner shelf longshore currents were controlled preferentially by tide, waves and wind, respectively. This clearly illustrates the potential of such remote method in quantifying the longshore current, in particular when considering its spatio-temporal variability and the need to cover longer scales.

6. Acknowledgments

References

Allen, J., Newberger, P., & Holman, R. (1996). The grand popo experiment, benin. *Journal of Fluid Mechanics*, *310*.

Almar, R., Bonneton, P., Michallet, H., Cienfuegos, R., Ruessink, B., & Tissier, M. (2014a). On the use of radon transform in studying nearshore wave dynamics. *Coastal Engineering*, *92*, 24–30.

11

284 Almar, R., Cienfuegos, R., Cataln, P., Michallet, H., Castelle, B., Bonneton,
285 P., & Marieu, V. (2012). A new breaking wave height direct estimator from
286 video imagery. *Coastal Engineering*, *61*, 24–30.

287 Almar, R., Du Penhoat, N., Y.and Honkonnou, Castelle, B., Laibi, R., Anthony,
288 E., N., S., Degbe, G., Chuchla, R., Sohou, Z., & Dorel, M. (2014b). The grand
289 popo experiment, benin. *Journal of Coastal Research*, *SI 70*, 651–656.

290 Almar, R., Kestenare, E., Reyns, J., Jouanno, J., Anthony, E., Laibi, R., Hemer,
291 M., Du Penhoat, Y., & Ranasinghe, R. (2015). Response of the gulf of guinea
292 coastline to anthropogenic and natural forcing, part1: Wave climate variabil-
293 ity and impacts on longshore sediment transport. *Continental Shelf Research*,
294 *110*, 48–59.

295 Anthony, E., & Blivi, A. (1999). Morphosedimentary evolution of a delta-
296 sourced, drift-aligned sand barrier-lagoon complex, western bight of benin.
297 *Marine Geology*, *158*, 161–176.

298 Blivi, A., Anthony, E., & Oyd, L.-M. (2014). Sand barrier development in the
299 bight of benin, west africa. *Ocean and Coastal Management*, *45*, 185–200.

300 Castelle, B., du Penhoat, Y., Almar, R., Anthony, E., Lefebvre, J., Laibi, R.,
301 Chuchla, R., Dorel, M., & Senechal, N. (2014). Flash rip dynamics on a high-
302 energy low-tide-terraced beach (grand popo, benin, west africa). *Journal of*
303 *Coastal Research*, *SI 70*, 633–638.

304 Chickadel, C., Holman, R., & Freilich (2003). An optical technique for the
305 measurement of longshore currents. *J. Geophys. Research: Oceans*, *108(C11)*,
306 73–82.

307 Copeland, A., Ravichandran, G., & Trivedi, M. (1995). Localized radon
308 transform-based detection of ship wakes in sar images. *IEEE Transactions of*
309 *Geoscience and Remote Sciences*, *33*, 35–45.

310 Cox, D., & Anderson, S. (2001). Satistics of intermittent surf zone turbulence
311 and observations of large eddies using piv. *Coastal Engineering*, *43*, 121–131.

12

312 De Vries, S., Hill, D., De Schipper, M., & Stive, M. (2011). Remote sensing of
313   surf zone waves using stereo imaging. *Coastal Engineering, 58(3)*, 239–250.

314 Dee, D. e. a. (2011). The era-interim reanalysis: configuration and performance
315   of the data assimilation system. *Q. J. R. Meteorol. Soc., 137*, 553597.

316 Feddersen, F. (2003). Observations of nearshore circulation: Alongshore unifor-
317   mity. *J. Phys. Oceanogr., 108*, DOI: 10.1029/2001JC001293.

318 Feddersen, F. (2014). The generation of surfzone eddies in a strong alongshore
319   current. *J. Phys. Oceanogr.,* .

320 Feeman, T. G. (2010). The mathematics of medical imaging, a beginner's guide.
321   *Springer Undergraduate Texts in Mathematics and Technology. Springer, New*
322   *York,* .

323 Haller, R., M.C. Dalrymple, & Svendsen, I. (2002). Experimental study of
324   nearshore dynamics on a barred beach with rip channels. *J. Geophys. Res.,*
325   *107*, 3061.

326 Haller, R., M.C. Dalrymple, & Svendsen, I. (2014). Rip current observations via
327   marine radar. *J. Waterway, Port, Coastal, and Ocean Engineering, 140(2)*,
328   115–124.

329 Heikkila, J., & Silven, O. (1997). A four-step camera calibration procedure
330   with implicit image correction. *Computer Vision and Pattern Recognition. In*
331   *Proceedings of the IEEE Computer Society Conference*, (pp. 1106–11012).

332 Holland, K., Holman, R., Lippmann, T., Stanley, J., & Plant, N. (2013). Prac-
333   tical use of video imagery in nearshore oceanographic field studies. *Oceanic*
334   *Engineering, 22(1)*, 81–82.

335 Holland, K., Puleo, J., & Kooney, T. (2001). Quantification of swash flows using
336   video-based particle image velocimetry. *Coast. Eng., 44(2)*, 6577.

337 Holman, R., & Haller, M. (2013). Remote sensing of the nearshore. *Annual*
338   *Review of Marine Science, 113*, 5–95.

13

₃₃₉ Kimmoun, O., & Branger, H. (2007). A particle images velocimetry investigation on laboratory surf-zone breaking waves over a sloping beach. *Journal of Fluid Mechanics*, *588*, 353–397.

Komar, P. (1998). Beach processes and sedmentation. *2nd edition, Prentice-Hall, NJ*, (p. 544 p).

Komar, P., & Inman, D. L. (1970). Longshore sand transport on beaches. *J. Geophys. Res.*, *75(30)*, 5914–5927.

Lippmann, T. (1970). Longshore currents generated byobliquely incident sea waves. *J. Geophys. Res.*, *75*, 6778–6789.

Lippmann, T., & Holman, R. (1990). The spatial and temporal variability of sand bar morphology. *J. Geophys. Research: Oceans*, *95(C7)*, 1157511590.

Lippmann, T., & Holman, R. (1991). Phase speed and angle of breaking waves measured with video techniques. *In N.C. Kraus, K.J. Gingerich, and D.L. Kriebel, editors, Coastal Sediments*, *SI 70*, 542–556.

MacMahan, J., Brown, J., & Thornton, E. (2009). Low-cost hand-held global positioning system for measuring surfzone currents. *Journal of Coastal Research*, *25(3)*, 744–754.

Mallat, S. (2008). *A Wavelet Tour of Signal Processing, Third Edition: The Sparse Way*. (3rd ed.). Academic Press.

Mole, M., Mortlock, T., Turner, I., Goodwin, I., Splinter, K., & Short, A. (2013). Capitalizing on the surfcam phenomenon: a pilot study in regional-scale shoreline and inshore wave monitoring utilizing existing camera infrastructure. *J. Coast. Res.*, *65*, 6778–6789.

Oltman-Shay, J., Howd, P., & Birkemeier, W. (1989). Shear instabilities of the mean longshore current: 2. field observations. *J. Geophys. Res.*, *94*, 18031–18042.

14

365 Plant, N., & Holman, R. (1997). Intertidal beach profile estimation using video
366   images. *Mar. Geol.*, *140*, 124.

367 Puloe, J., Farquharson, G., Frasier, S., & Holland, K. (2003). Comparison of
368   optical and radar measurements of surf and swash zone velocity fields. *J.*
369   *Geophysical Res.*, *108*, C3 3100.

370 Putrevu, J., U. Oltman-Shay, & Svendsen, I. (1995). Intertidal beach profile
371   estimation using video images. *J. Geophysical Res.*, *100*, 16119–16130.

372 Radon, J. (1917). Uber die bestimmung von funktionen durch ihre integralwerte
373   l'angs gewisser mannigfaltigkeiten. *Akad. Wiss.*, *69*, 262–277.

374 Ramm, A., & Katsevich, A. (1996). *The Radon Transform and Local Tomogra-*
375   *phy*. Taylor & Francis.

376 Schoonees, J., & Theron, A. (1993). Review of the field database for longshore
377   sediment transport. *Coastal Engineering*, *19*, 1–25.

378 Splinter, K., Davidson, M., Golshani, A., & Tomlinson, R. (2012). Climate
379   controls on longshore sediment transport. *Continental Shelf Research*, *48*,
380   146–156.

381 Stockdon, H. F., & Holman, R. (2000). Estimation of wave phase speed and
382   nearshore bathymetry from video imagery. *Journal of Geophysical Research*
383   *- Oceans*, *105*, null+. URL: `http://dx.doi.org/10.1029/1999jc000124`.

384 Thornton, E., & Guza, R. (1986). Surf zone longshore currents and random
385   waves: Field data and models. *J. Phys. Oceanogr.*, *16*, 1165–1178.

386 Yoo, J., Fritz, H., Haas, K., Work, P., & Barnes, C. (2009). Waves swash
387   velocity estimation using ridgelet transform. *In: 9th Int. Conf. Electronic*
388   *Meas. and Instr. ICEMI 09*, (pp. 1078–1081).

389 Yoo, J., Fritz, H., Haas, K., Work, P., & Barnes, C. (2011). Depth inversion in
390   the surf zone with inclusion of waves non-linearity using video-derived celerity.
391   *J. Waterw. Port Coastal Oc. Eng.*, *137(2)*, 95–106.
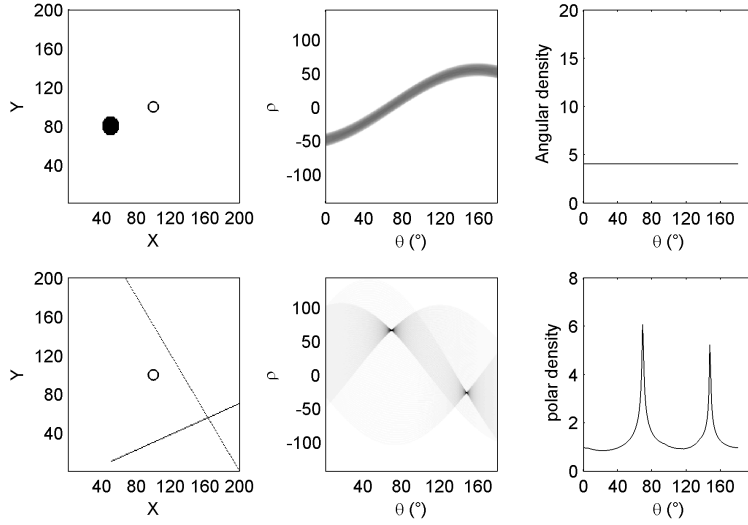
15

List of Figures

16

17

Figure 1: Radon transform (RT) practical use. RT of a disk and inclined lines in upper and lower panels respectively, and from left to right: original fields, RT in polar space, and resulting integrated angular density.
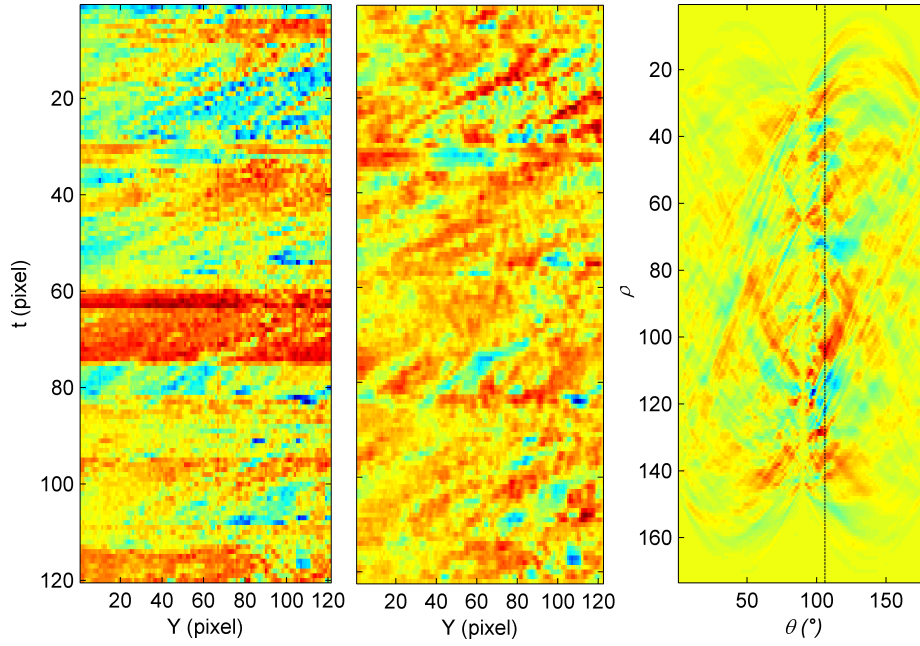
Figure 2: Illustration on the separation of waves from drifting features in longshore spatio-temporal images using the RT. a) mixed wave-current intensity timestack, b) wave-filtered current timestack and c) Polar space visualization of timestack in b). Grand Popo spatio-temporal longshore image from video, $dx = 0.25m/pix$, $dt = 0.5s$. Dashed line at $\theta = 106°$ shows the variance maximum, or dominant velocity ($V = 0.14m/s$).
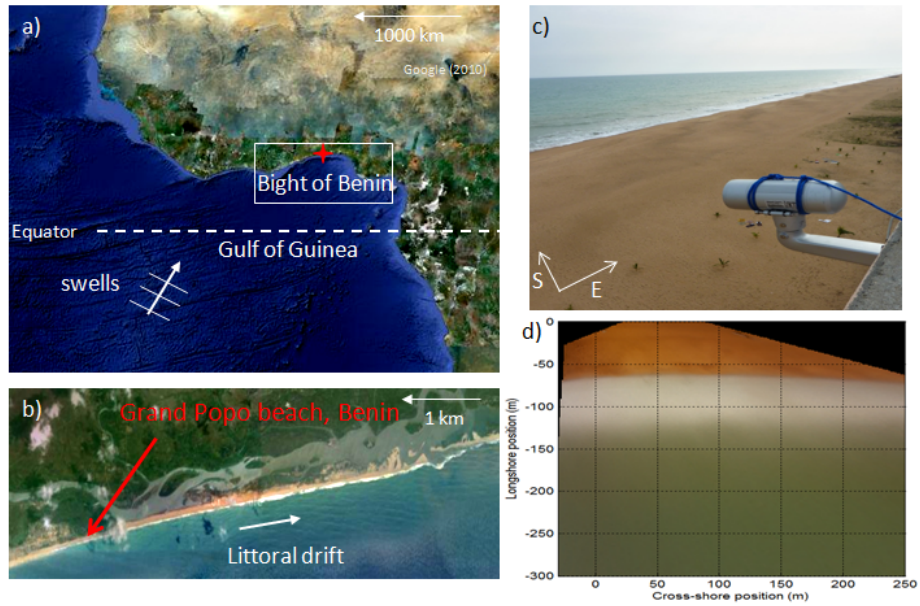
Figure 3: Grand Popo beach (6.2°N, 1.7°E), in the Bight of Benin, Gulf of Guinea West Africa (a-b). c) Permanent video camera, on a 15-m high semaphore and d) rectified 15-min averaged image from video system.
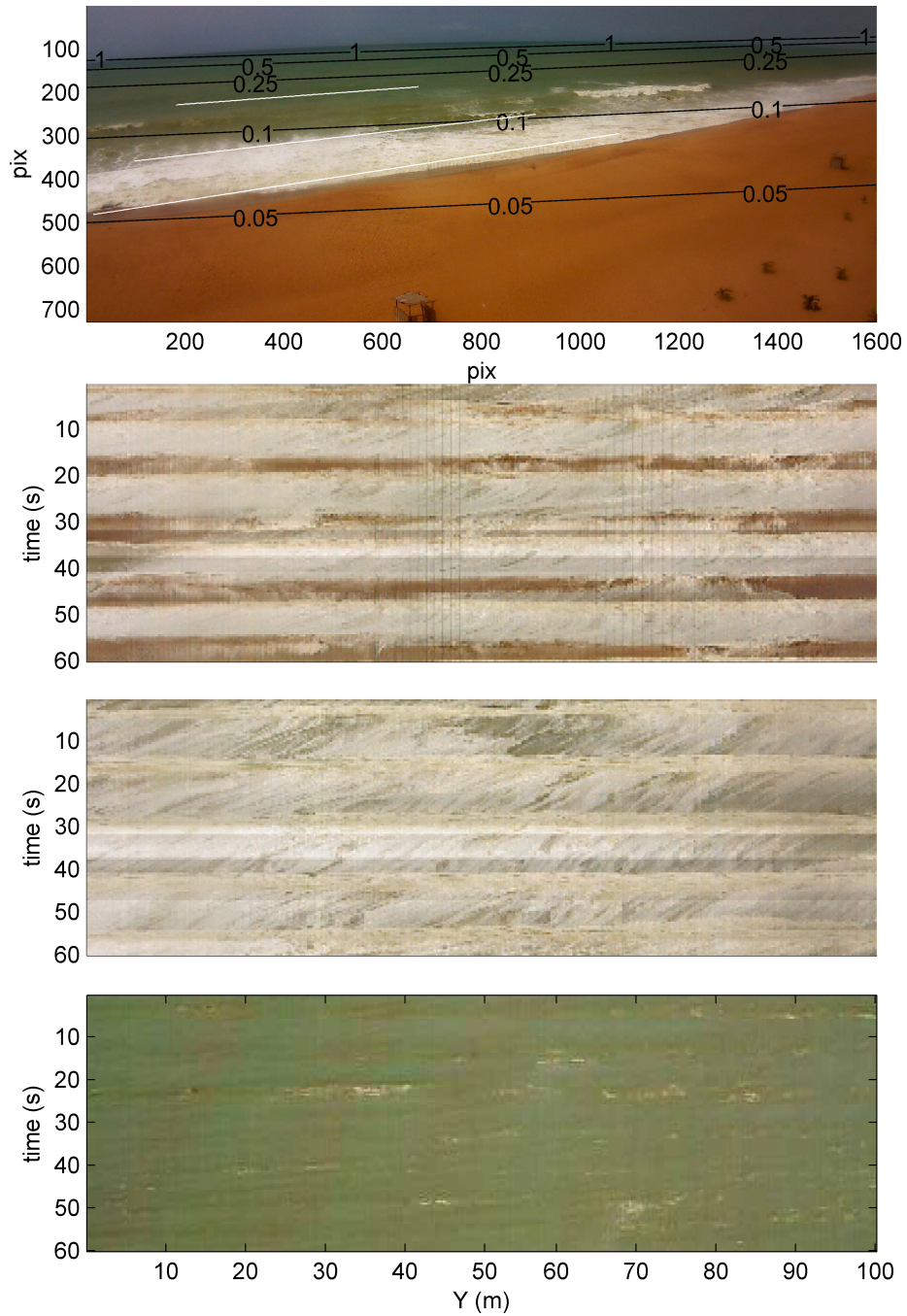
Figure 4: Instant video image with superimposed black iso-contours of pixel footprint (m/pix) in the longshore direction and in white location of 100-m long longshore spatio-temporal transects, b) in the swash, c) surf and d) inner shelf zones. Drifting features at these 3 zones are clearly visible.

21
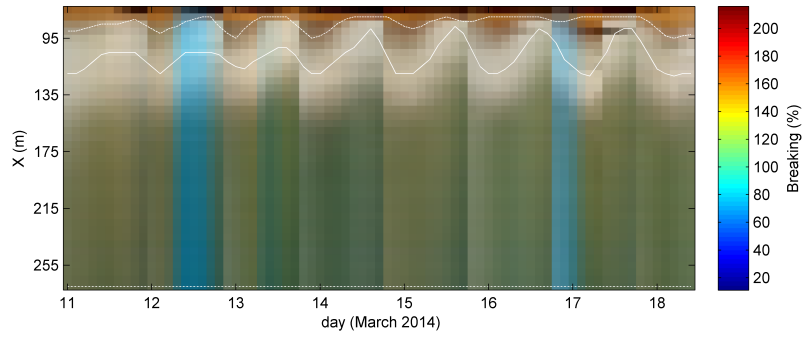
Figure 5: Cross-shore timestack derived from time-averaged images. Time-varying swash and surfzone locations used in the RT method are superimposed. Inner shelf location is taken constant.
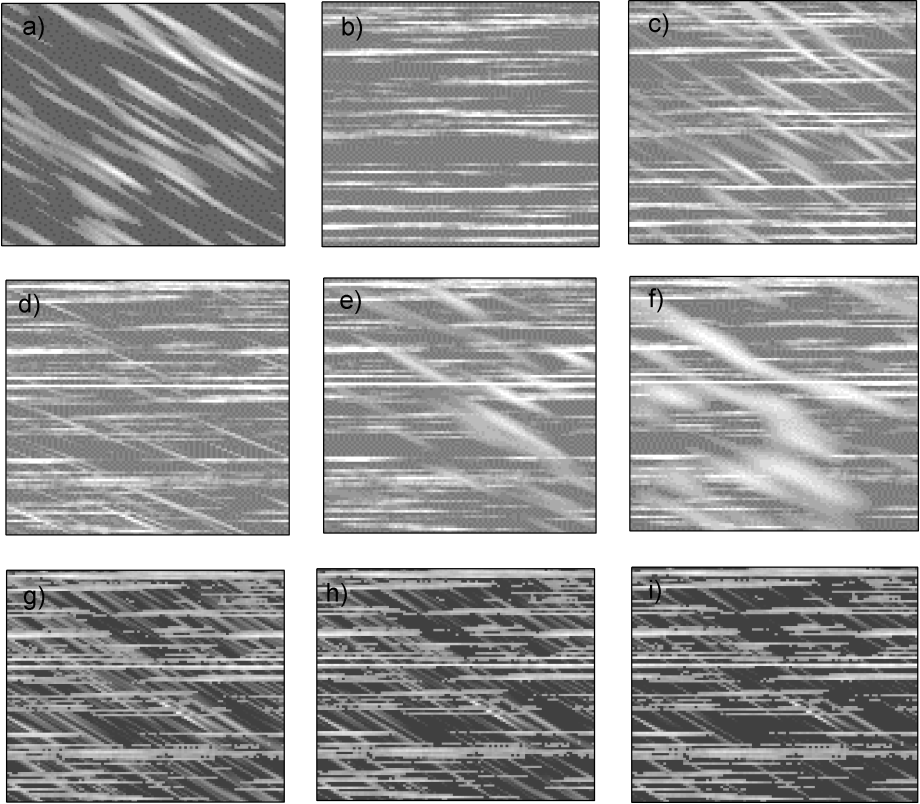
Figure 6: Examples of synthetic test cases, a-c): from left to right, anisotropic random Gaussian currents and wave fields and a combination of both. Random Gaussian current field with in d-f) from left to right, correlation ratio of 0.05, 0.15 and 0.25, and in g-i) from left to right, thresholds on kept pixels of 30%, 50% and 70%.
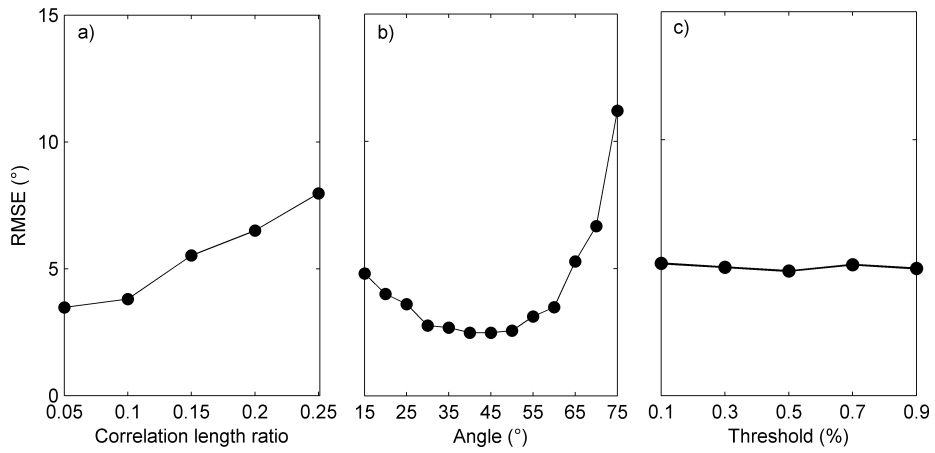
Figure 7: Sensitivity analyze on RT skills in retrieving current velocity from synthetic Gaussian random current fields. RMSE error as a function of a) Correlation length ratio (isotropy), b) threshold on kept information (in percent of pixels not changed) and c) orientation (or velocity).
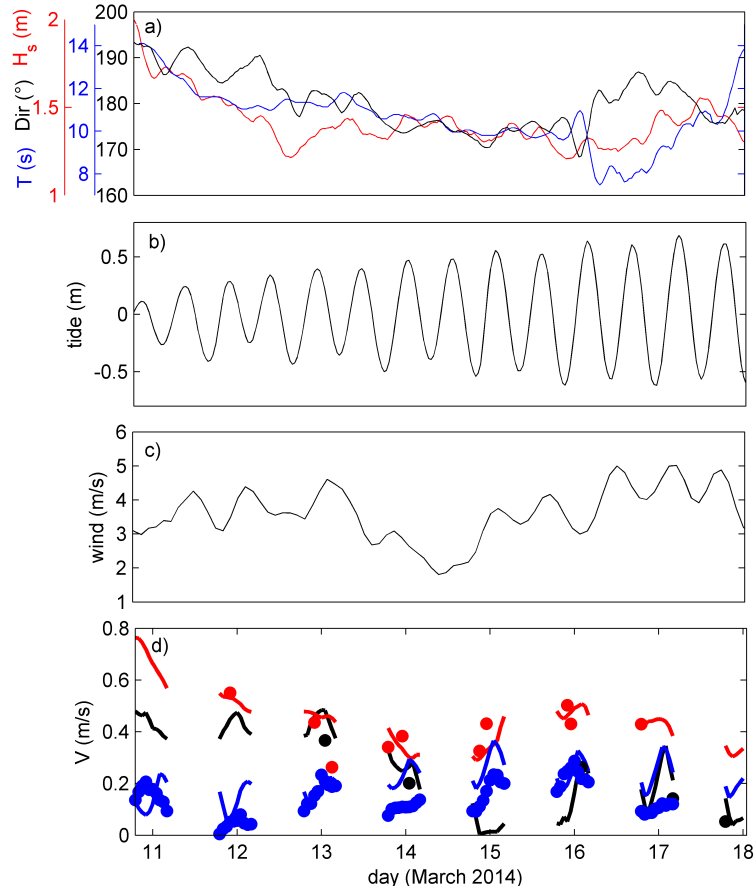
Figure 8: Forcing and longshore current during Grand Popo 2014 experiment. a) Waves (Hs, T, Dir) and b) tide measured by ADCP, c) observed wind at Cotonou airport d) Comparison of co-localized video (continuous line) and in-situ current measurements in the surf zone (red), swash (black) and inner shelf (blue), from drifters, ADV and ADCP, respectively.
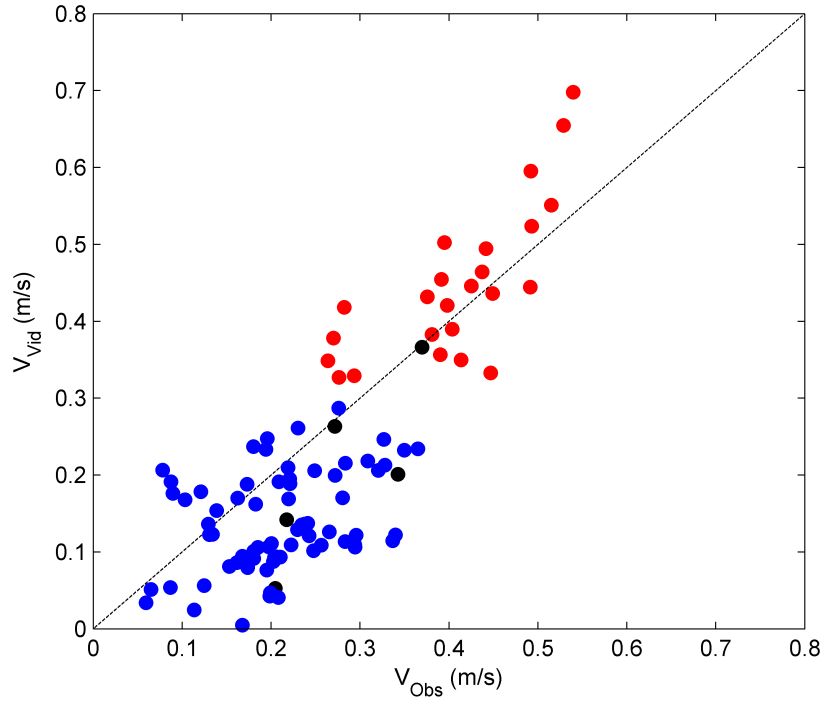
Figure 9: Video-derived versus in-situ current, in the surf zone (red), swash (black) and inner shelf (blue), from drifters, ADCP and ADV, respectively.
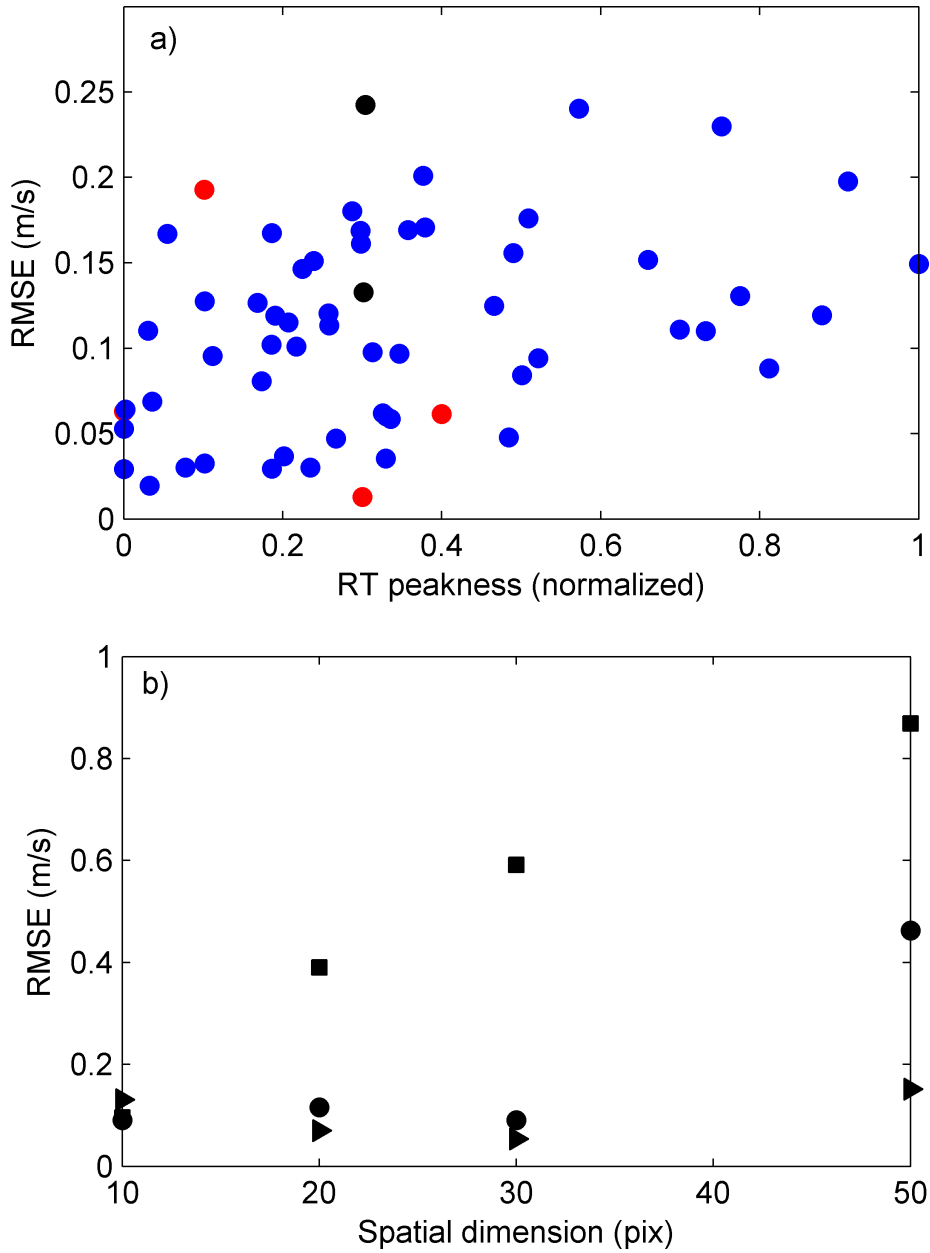
Figure 10: RT-method error as a function of a) RT-transform peakness (width of the peak in polar space) and b) resolution (0.1 m/pixel (triangles), 0.2 m/pixel (circles) and 0.4 m/pixel (squares)) and spatial dimension (pixels). In a) are shown estimates for the inner shelf (blue), surf- (red) and swash-zones (black).
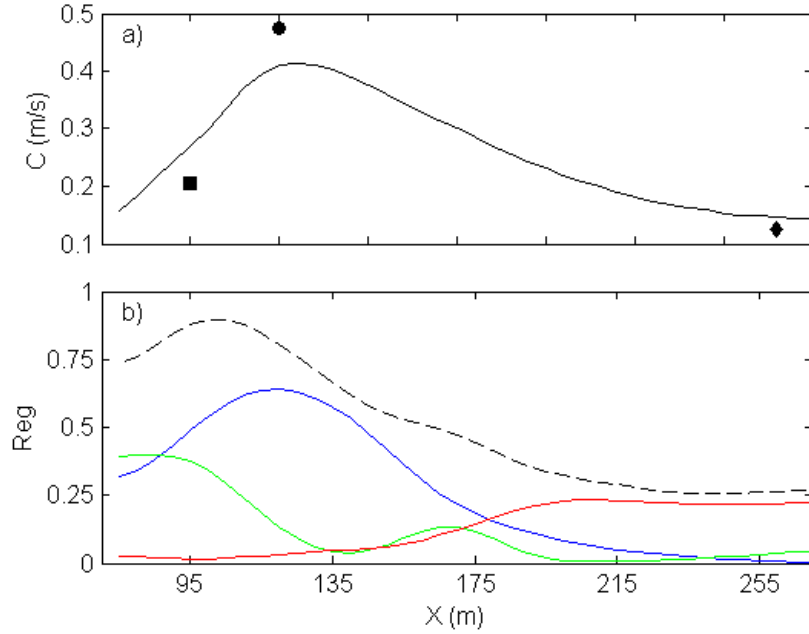
Figure 11: a) Cross-shore profile of longshore current derived from the RT (continuous line), ADV in the swash (square), drifters in the surf (circle) and ADCP (diamond), averaged when both video and in-situ measurements were available. b) Percentage of variance of RT-derived current timeseries at each location retrieved from waves and tide (ADCP) and wind (80-km distant Cotonou airport - 500 m from coastline).